Fuel 405 (2026) 136427

Contents lists available at ScienceDirect

Fuel

journal homepage: www.elsevier.com/locate/fuel

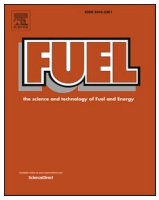

Full Length Article

Experimental and kinetic study of non-equilibrium plasma driven NH_3 decomposition

Shuming Li, Huanrui Guo, Geyuan Yin *, Erjiang Hu, Zuohua Huang

State Key Laboratory of Multiphase Flow in Power Engineering, Xi'an Jiaotong University, Xi'an 710049, People's Republic of China

ARTICLE INFO

Keywords:
Ammonia decomposition
Chemical kinetic model
Dielectric barrier discharge
Non-equilibrium plasma

ABSTRACT

This study establishes the first low temperature kinetic model for plasma-assisted ammonia decomposition based on the experiment in a dielectric barrier discharge reactor, addressing the limitations in both conventional combustion chemical kinetics models and plasma models and improves the model prediction at low temperatures. By integrating the diagnostics with kinetic modeling, a multi-scale framework is developed which explicitly couples electron-impact reactions with excited Ar* pathways. The model uniquely achieves 53.4 % higher predictive accuracy than combustion models through systematic validation against measured concentrations. Key mechanistic insights reveal: (i) Plasma-driven processes predominantly govern the initial decomposition of NH_3 and subsequent H_2 formation, with direct electron-impact dissociation of NH_3 accounting for over 95 % of the total H_2 yield; (ii) Ar* serves dual roles as energy carrier (11.55 eV excitation) and reactive collision partner, enabling efficient energy transfer via quenching-induced NH_3 decomposition ($Ar^*+H+NH_3 \rightarrow NH_2+2H+Ar$); (iii) N_2 formation proceeds through NH_2 dimerization ($NH_2+NH_2=N_2H_4$) followed by sequential H-abstraction dehydrogenation ($N_2H_4 \rightarrow N_2H_3 \rightarrow N_2H_2 \rightarrow NNH \rightarrow N_2$). These findings provide fundamental guidelines for designing plasma-assisted NH_3 decomposition, demonstrating the viability of low-temperature on-demand hydrogen production with enhanced energy efficiency.

1. Introduction

The excessive carbon emissions resulting from widespread fossil fuel utilization have triggered a global greenhouse effect, driving significant attention toward ammonia and hydrogen energy systems. While hydrogen stands as an ideal zero-carbon fuel due to its complete combustion yielding only water, practical implementation faces critical barriers including challenges in liquefaction (requiring temperatures below −253 °C) and safety risks from high flammability and explosion potential.

Ammonia utilization for hydrogen production has emerged as a strategic solution to these limitations [1]. Conventional thermal decomposition methods demand sustained high temperature with long system activation periods and substantial energy consumption, rendering them unsuitable for on-demand hydrogen generation. In contrast, plasma-assisted decomposition presents a promising alternative pathway. Plasma technology not only exhibits flexible start-stop operation but also demonstrates adaptability to the intermittent and fluctuating nature of renewable energy generation, thereby enabling efficient utilization of low-cost surplus and off-peak electricity [2].

This emerging field has attracted substantial research attention, with extensive experimental and computational investigations being conducted to elucidate the underlying mechanisms and optimize system performance. Alexander et al. [3] qualitatively detected ammonia decomposition products under ambient temperature and atmospheric pressure conditions using emission and absorption spectroscopy. Through application of the Lambert-Beer law, they quantitatively determined the N_2H_4 concentration. Their findings demonstrated that the primary stable products generated Ar/NH_3 gas mixtures at atmospheric pressure within a dielectric barrier discharge (DBD) reactor were H_2, N_2, and N_2H_4.The first experimental study of plasma-assisted ammonia combustion was conducted by Sun et al [4]. The results showed that plasma can simultaneously extend the lean blowoff limits of ammonia flames and reduce NO_x emissions, however, no specific kinetic analysis was performed. Zhong et al. [5] investigated the non-equilibrium reaction pathway of ammonia oxidation at 4 kPa by combining in-situ laser diagnostics with plasma modeling, and showed that non-equilibrium plasma controls the ammonia oxidation process

* Corresponding author.
E-mail address: yingeyuan@xjtu.edu.cn (G. Yin).

https://doi.org/10.1016/j.fuel.2025.136427
Received 22 April 2025; Received in revised form 26 June 2025; Accepted 30 July 2025
Available online 5 August 2025

through electron collisional dissociation and quenching of excited state species. Zhang et al. [6] performed plasma-assisted ammonia cracking and oxidation experiments at low temperature(350 K) and low pressure (8 kPa), and calculated the mole fraction of H_2, N_2 and NH_3 based on a combustion model of Glarborg et al [7] which focuses on the prediction of ammonia flames, shock tubes and flow reactors at high temperatures (>1000 K).

This work addresses the insufficient research on plasma-assisted ammonia decomposition under low temperature: (1) Current experimental investigations are predominantly focused on low-pressure conditions, with a notable absence of data under atmospheric pressure and elevated pressure, result in excessive E/N ratios and inefficient electron energy distribution; (2) Existing models, primarily based on combustion kinetics, demonstrate inadequate predictive capabilities for plasma-driven ammonia decomposition at ambient temperatures; (3) Prevailing plasma reaction mechanisms lack comprehensive inclusion of critical electron impact processes, compromising their physicochemical accuracy. Therefore the following works has been carried out in this paper: (1) DBD discharge experiments under nanosecond pulsed discharge excitation were carried out at atmospheric pressure and room temperature under appropriate E/N ratio range, and the concentrations of products under plasma were measured; (2) A novel and detailed modified model is developed and experimentally validated, which is able to accurately predict the ammonia decomposition with plasma assisted at low temperature and path analysis for excited state and key radicals in the discharge and afterglow process are provided; (3) Based on the above pathways, the influence of plasma on NH_3 consumption and H_2 formation is discussed and revealed.

2. Experimental and numerical method

2.1. Experimental setup

The experiments were conducted in a dielectric coaxial DBD reactor under atmospheric and room temperature. The experimental installation used in this study is presented in Fig. 1. Flow rates of NH_3 and Ar are individually controlled by mass flow controllers and thoroughly mixed before the DBD reactor. The reactor consists of a quartz tube integrated with a coaxial stainless-steel electrode inside and a concentric copper electrode affixed to the quartz tube. This reactor measures 450 mm in length and 15 mm in inner diameter. The high-voltage electrode spans 30 mm, leading to a reaction volume of 4.71 cm^3 and a residence time of 0.28 s in the discharge region. The residence time is calculated as:

$$\tau = \frac{V}{F} = \pi(R^2 - r^2)L(F_N \frac{T}{273.15}\frac{0.1}{p})^{-1} \quad (1)$$

Where τ(min) is the residence time, V(cm^3) is the volume of the flow reactor, F_N (SCCM) is the flow rate under standard conditions, F (ml/min) is the practical flow rate, T (K) is the practical temperature and p (MPa) is the practical pressure.

The gas temperature at the reaction region was monitored using a K-type thermocouple at the end of the discharge region to avoid plasma interference. And within the 30 mm reaction zone, the system temperature remains constant after the discharge reaches steady state. The system utilizes a nanosecond-pulsed power supply to generate plasma discharges within the setting voltage range of 0–20 kV, the setting frequency range of 1–100 kHz and the pulse width setting range of 0–1 ms. And the square waveform was applied for all the experimental conditions with pulse voltage, pulse frequency and pulse width of 3500–6500 V, 20 kHz and 150 ns, respectively. The discharge voltage and current curves and NH_3, NO, N_2O and NO_2 data collection are shown in Supplementary material.

The gas mixtures consist of 1 % NH_3/99 % Ar with a total flow rate of 1000 SCCM. The choice of diluent gas can indeed influence the experimental results. Mao et al. [8] have investigated the difference of diluent gases (He, Ar, N_2). The results show that Ar is the most easily ionized gas, producing the highest current upon breakdown, followed by He. This behavior is due to the fact that Ar has a lower ionization potential (~15.8 eV) compared to He (24.5 eV). The concentrations were analyzed by gas chromatograph (GC) equipped with a thermal conductivity detector (TCD) and Fourier transform infrared (FTIR) spectroscopy. The detection limit for species analyzed using the TCD and FTIR was 10 ppm causing 1 % uncertainty for major species like NH_3, H_2, and N_2. Additionally, the random error of the measurement is less than 5 % on the basis of test repeatability. In general, these factors result in an uncertainty of about 10 % for the species as mentioned before [7].

2.2. Numerical method

A coupled plasma and combustion chemistry solver (CPCC) [9] by combing the ZDPlaskin code [10]with combustion dynamics solver CHEMKIN [11] has been developed on the basis of Hybrid Plasma and

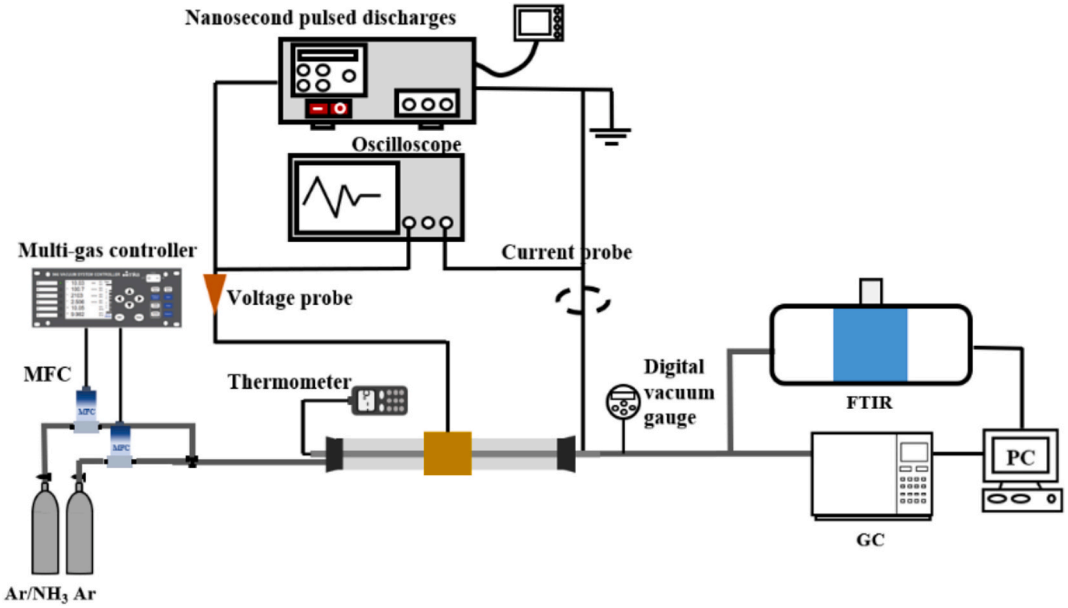

Fig. 1. The schematic diagram of the experimental setup.

Combustion code [12]. Electron collision reaction rates were obtained by solving the Boltzmann equation by the BOLSIG + solver [13].In this work, we use the CPCC code to simulate the nanosecond pulsed discharge-assisted methanol decomposition and analyze the microscopic chemical reaction kinetics. The Poisson equation is not solved in this model, so it is assumed that the deposited energy in plasma is an adjustable parameter that controls the discharge duration.

3. Chemical kinetic model

Based on the existing combustion model, a detailed mechanism of plasma-assisted NH_3 decomposition is developed which improves low-temperature computational accuracy by optimizing rate constants. The mechanism consists of two parts, the ground state kinetic mechanism and the plasma kinetic mechanism, with 72 components and 250 reactions. Major updates are made to the ground state kinetic mechanism, as detailed below. In addition, thermodynamic properties were updated using the database from Glarborg et al [6] (see Appendix).

3.1. Nh_x chemistry

The key reaction in traditional ammonia pyrolysis is $NH_2 + H + M{=}NH_3 + M$ (R1). Alturaifi et al. [14] showed that NH_2 and H radicals were rapidly generated during the first few microseconds of NH_3 pyrolysis, followed by the rapid formation of intermediates such as NH, N, and N_2H_2 from the two mixtures. And H radicals are consumed by the hydrogen abstraction reaction $NH_3 + H{=}NH_2 + H_2$, with a consequent decrease in the rate of H production. Davidson et al. [15] first reported the rate constant for this reaction, expressed as 2.2×10^{16} exp(−93470/RT) $cm^3{\cdot}mol^{-1}{\cdot}s^{-1}$, which is applicable over a temperature range of 1740–3300 K with an uncertainty of 15 %. This result has been subsequently cited by Otomo et al. [16], Song et al. [17], Konnov et al. [18], and Zhang et al. [19] in their follow-up studies. Furthermore, Oliver et al. [20] developed their own kinetic model based on the NH_3 model proposed by Dagaut et al. [21] and the NNH model constructed by Klippenstein et al. [22]. Alturaifi et al. [14] demonstrated that the mechanism developed by Davidson et al. [15] is the only model specifically tailored for NH_3 pyrolysis, which was validated and refined against the experimental data from their study. The refinements included the addition of reactions involving NH_2, NH, and N_2H_2; the incorporation of reactions for N_2H_3, N_2H_4, and H_2NN; and the adoption of recent thermodynamic data as well as updated rate constants for individual reactions. Glarborg et al. [23] validated the existing rate constants for this reaction across a wide range of low pressures and temperatures, based on the results from Klippenstein et al. [22], showing excellent agreement with experimental values at lower temperatures. The experimental and theoretical computational results are presented in Fig. 2, and the computational results from Glarborg et al. [23] were adopted in this study. Detailed chemical reaction rate constants and their sources are listed in Table 1.

The chain propagation reaction $NH_3 + H{=}NH_2 + H_2$ (R2) has been extensively studied over a wide temperature range (as shown in Fig. 3). Experimental measurements were conducted by Ko et al. [24] at low temperatures and by Michael et al. [32,33] at intermediate temperatures. Numerous computational and fitting results [23,34–36] have demonstrated excellent agreement with the experimental data. In this study, the fitting data from Ko et al. [24] were selected.

NH_2 is primarily consumed through reactions with radicals such as H and NH. At high temperatures, NH_2 can dissociate into NH and H via the three-body reaction $NH + H + M{=}NH_2 + M$ (R3). Deppe et al. [37] reported the only high-temperature experimental measurements, while Glarborg et al. [23] fitted the reaction rates at low temperatures. However, the reactions of NH_2 with H and NH dominate its consumption pathway. As shown in Fig. 4(a), experimental data on the rate constant for the reaction $NH_2 + H{=}NH + H_2$ (R4) are relatively limited. In the low-temperature range, only Bahng et al. [38] provided experimental

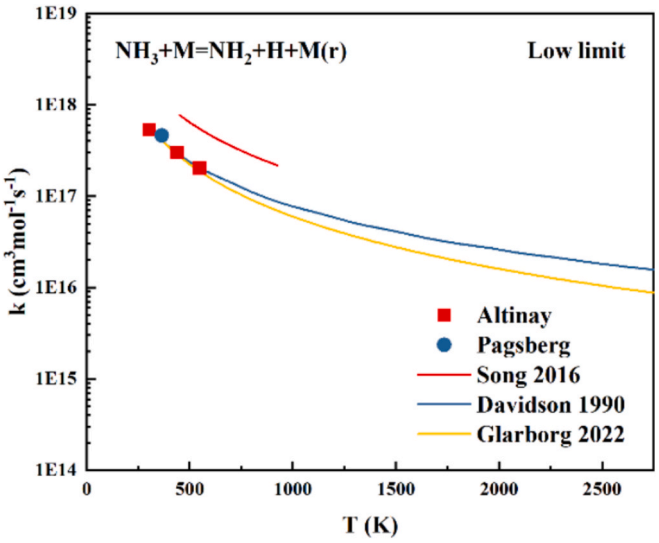

Fig. 2. Low pressure limit rate constant of $NH_2 + H + M{=}NH_3 + M$ as a function of temperature. Symbols denote experiment and lines denote calculation.

measurements, while Davidson et al. [15], Fontijn et al. [39], Rohrig et al. [40], and Dove et al. [40] reported relevant experimental data at intermediate and high temperatures. The rate constants proposed by Linder et al. [25] were compared with experimental results in the range of 1100–1300 K and were adopted by Song et al. By comparing the fitting results from Linder et al. [25], Glarborg et al. [23], and Davidson et al. [15], it was found that the rate constants provided by Glarborg et al. [23] offer better agreement with low-temperature experimental data. Therefore, this study adopts the rate constants from Glarborg et al. [23] to more accurately predict ammonia decomposition behavior at low temperatures.

Klippenstein et al. [25] demonstrated that for the reaction $NH_2 + NH \rightarrow$ Products, the pathway $NH_2 + NH{=}N_2H_2 + H$ (R6) exhibits greater kinetic dominance over the temperature range of 200–2500 K, while the branching ratio of the alternative pathway $NH_2 + NH{=}NH_3 + N$ (R7) is only about 4 %. The rate constants proposed by Davidson et al. [15] show better agreement with experimental data at low temperatures (as shown in Fig. 4(b)), and thus, their values are adopted in this study.

For the reaction $NH_2 + NH_2 \rightarrow$ Products, Dean et al. [27] demonstrated that at low temperatures, the recombination of NH_2 primarily yields N_2H_4, followed by $H_2NN + H_2$, while at high temperatures, the pathway leading to $NH_3 + NH$ becomes dominant. Klippenstein et al. [25] suggested that the internal energy of the pathway $N_2H_3 + H$ is significantly high, resulting in a relatively small rate constant except at extremely high temperatures. They also predicted the rate constants for the pathways $H_2NN + H_2$ and $N_2H_2 + H_2$, which were found to be considerably lower than that of the dehydrogenation reaction $NH_3 + NH$. The specific pathways for the $NH_2 + NH_2$ reaction remain inconclusive, and thus, this study adopts the results from Klippenstein et al. [25]. See Fig. 5.

For the NH radical, its consumption is primarily governed by reactions with other radicals, such as H and NH. The model of Meng et al. [45] uses a constant value of 3.0E13 $cm^3mol^{-1}s^{-1}$. By comparing theoretical calculations of the reaction $NH + H{=}N + H_2$ with experimental data in Fig. 6(a), it was found that the predictions by Zhang et al. [19] exhibit excellent agreement across the entire temperature range. Therefore, this study adopts the results from Zhang et al. [19].

Next, the reaction NH + NH → products is analyzed. As shown in Fig. 6(b), Klippenstein et al. [25] illustrated the reaction pathways of NH + NH based on CCSD(T)/CBS//CCSD(T)/aug-cc-pvtz theoretical calculations. The study revealed that the addition reaction of NH exhibits no barrier on either the singlet or triplet states, whereas the

Table 1
List of reactions in the proposed ground mechanism in Arrhenius expression $k = AT^{n} \exp(-E_a/(RT))$. Units are mol, cm, s, cal.

	Reactions	A	n	E_a	Source
R1	$NH_2 + H + M = NH_3 + M$	1.5E14	0.167	0	[6]
R2	$NH_3 + H = NH_2 + H_2$	7.3E13	0	13,750	[24]
R3	$NH_2 + M = NH + H + M(r)$	1.2E25	−2.71	0	[6]
R4	$NH_2 + H = NH + H_2$	5.1E08	1.50	3700	[6]
R5	$NH_2 + N = N_2 + H + H$	7.0E13	0	0	[6]
R6	$NH_2 + NH = N_2H_2 + H$	1.5E15	−0.5	0	[15]
R7	$NH_2 + NH = NH_3 + N$	9.6E03	2.46	107	[6]
R8	$NH_2 + NH_2 = NH_3 + N$	5.6E0	3.53	552	[25]
R9	$NH_2 + NH_2 = N_2H_2 + H_2$	1.7E08	1.02	11,783	[25]
R10	$NH_2 + NH_2 = H_2NN + H_2$	7.2E04	1.88	8802	[25]
R11	$NH_2 + NH_2 + M = N_2H_4 + M$	5.6E14	−0.414	66	[25]
R12	$NH + M = N + H + M$	1.8E14	0	74,800	[6]
R13	$NH + H = N + H_2$	1.65E11	0.71	931	[19]
R14	$NH + N = N_2 + H$	8.7E13	0	186	[26]
R15	$NH + NH = N_2H_2$	6.26E13	−0.036	−160.9	[25]
R16	$NH + NH = NNH + H$	6.2E13	−0.036	−161	[23]
R17	$NH + NH = N_2 + H + H$	5.634E13	−0.036	−160.9	[25]
R18	$NH + NH = N_2 + H_2$	6.26E12	−0.036	−160.9	[25]
R19	$NH + NH = NH_2 + N$	5.7E-1	3.88	172	[25]
R20	$N_2H_2 + M = NNH + H + M$	1.9E27	−3.05	66,107	[27]
R21	$N_2H_2 + H = NNH + H_2$	1.1E14	0	3128	[6]
R22	$N_2H_2 + H = N_2H_3$	1.3E14	0	3871	[6]
R23	$N_2H_2 + NH = NNH + NH_2$	2.4E6	2.0	−1192	[23]
R24	$N_2H_2 + NH_2 = NNH + NH_3$	2.71E5	2.226	−1030	[19]
R25	$N_2H_2 + N_2H_2 = NNH + N_2H_3$	1.0E13	0	9935	[19]
R26	$N_2H_2 + N_2H_3 = NNH + N_2H_4$	1.0E13	0	6028	[28]
R27	$N_2H_3(+M) = N_2H_2 + H(+M)$	1.28E11	0.819	41,800	[28]
R28	$N_2H_3 + H = N_2H_2 + H_2$	7.476E3	2.796	4684	[29]
R29	$N_2H_3 + H = H_2NN + H_2$	6.243E6	1.89	246.6	[29]
R30	$N_2H_3 + H = NH_2 + NH_2$	7.926E14	−0.189	521.5	[29]
R31	$N_2H_3 + NH = N_2H_2 + NH_2$	2E13	0	0	[30]
R32	$N_2H_3 + NH_2 = N_2H_2 + NH_3$	6.08E-1	3.574	1190	[29]
R33	$N_2H_3 + NH_2 = H_2NN + NH_3$	1.11E1	3.08	211	[29]
R34	$N_2H_3 + N_2H_3 = N_2H_4 + H_2NN$	9.325E-8	4.97	6249.5	[29]
R35	$N_2H_4 = H_2NN + H_2$	1.4E14	0	74,911	[23]
R36	$N_2H_4 = N_2H_2 + H_2$	5.2E38	−7.84	67,100	[19]
R37	$N_2H_4 + H = N_2H_3 + H_2$	7.0E12	0	2500	[31]
R38	$N_2H_4 + H = NH_3 + NH_2$	3.0E06	2.07	8012	[23]
R39	$N_2H_4 + N = N_2H_3 + NH$	1E10	0	2008	[28]
R40	$N_2H_4 + NH = N_2H_3 + NH_2$	1E9	1.5	2000	[28]
R41	$N_2H_4 + NH_2 = N_2H_3 + NH_3$	1.8E6	1.71	−1387	[28]
R42	$H_2NN = N_2H_2$	1.3E14	0	46,931	[6]
R43	$H_2NN = N_2 + H_2$	2.5E14	0	52,785	[6]
R44	$H_2NN = NNH + H$	3.4E26	−4.83	46,228	[22]
R45	$H_2NN + H = NNH + H_2$	4.8E8	1.5	−894	[27]
R46	$H_2NN + H = N_2H_2 + H$	1.8E10	0.97	4470	[22]
R47	$H_2NN + NH_2 = NH_3 + NNH$	1.8E6	1.94	−1152	[27]
R48	$NNH = N_2 + H$	1E9	0	0	[22]
R49	$NNH + H = N_2 + H_2$	1.0E14	0	0	[28]
R50	$NNH + N = N_2 + NH$	3.0E13	0	2000	[18]
R51	$NNH + NH = N_2 + NH_2$	5.0E13	0	0	[15]
R52	$NNH + NH_2 = N_2 + NH_3$	5.0E13	0	0	[15]
R53	$NNH + NNH = N_2 + N_2H_2$	1.0E13	0	10,000	[18]

dehydrogenation reaction leading to $NH_2 + N$ possesses barriers on both the triplet and quintet states. Consequently, the addition reaction dominates the kinetics. Furthermore, the energy barrier for the singlet state pathway NNH + H is significantly lower than the saddle point of the $N_2 + H_2$ pathway and is barrierless, making reaction (R16) more important than reaction (R18).

3.2. N_2H_x chemistry

Linder et al. [49] employed variational transition state theory calculations to determine the rate constants for the reactions $N_2H_2 + H = NNH + H_2$ (R21) and $N_2H_2 + NH_2 = NNH + NH_3$ (R24) over a temperature range of 300–3000 K. The rate constant for the reaction $N_2H_2 + H = NNH + H_2$ was cited by Konnov et al. [18]. Results from other studies are similar, with differences within one order of magnitude. Zheng et al. [50] provided the branching ratios for the dehydrogenation reaction $N_2H_2 + H = NNH + H_2$ (R21) and the addition reaction $N_2H_2 + H = N_2H_3$ (R22). Theoretical calculations revealed that the classical barrier height for the addition reaction is approximately 1 kcal/mol lower than that of the dehydrogenation reaction. However, due to vibrational adiabaticity, the rate of the addition reaction is lower than that of the dehydrogenation reaction. At 200 K, the branching ratio between the dehydrogenation and addition reactions is 3.5, decreasing to 1.2 at 1000 K and further to 1.06 at 1500 K. Therefore, under the low-temperature conditions considered in this study, the dehydrogenation reaction rate is dominant. Fig. 7 compares the rate constants from various models, and the rate and branching ratio for the $N_2H_2 + H$ reaction in this model are based on the results from Zheng et al. [50].

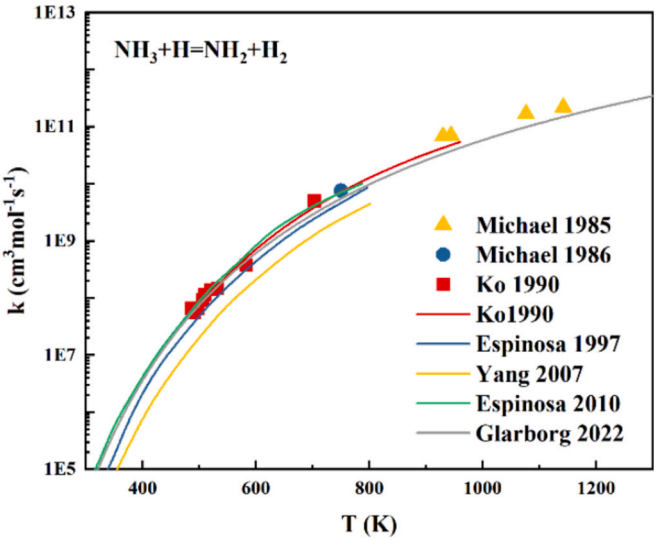

Fig. 3. Rate constant of $NH_3 + H = NH_2 + H_2$ as a function of temperature. Symbols denote experiment and lines denote calculation.

Miller et al. [30] incorporated reaction (R23) into the mechanism, demonstrating that the experimental results are insensitive to this value. The reaction $N_2H_2 + NH_2 \rightarrow$ products exhibits two branching pathways, with reaction (R24) being the dominant one. Linder et al. [49] conducted theoretical calculations across the entire temperature range, and their results have been referenced in the models of Glarborg et al. [23] and Song et al. [17]. Pascal et al. [29] performed the most recent theoretical calculations in the temperature range of 250–2500 K, which were subsequently incorporated into the model by Zhang et al. [19]. Our model also adopts this result. Although there have been numerous theoretical studies on the reaction $N_2H_3 + H/NH_2 \rightarrow$ products, the results vary within four orders of magnitude. This model adopts the latest research findings from Pascal et al. [29].

For the hydrogen abstraction reactions of N_2H_4, reaction (R37) predominates over (R38) as the main pathway. Fig. 8(a) compares experimental results with theoretical calculations at low temperatures, showing that the results from Glarborg et al. [31] exhibit the best agreement. Therefore, this study adopts their results.

There have been numerous computational results for reaction (R41), and Fig. 8(b) compares the existing experimental values with simulated values. Significant discrepancies are observed among the models, and this study adopts the results from Konnov et al. [18], which demonstrate better agreement with the experimental data.

3.3. Plasma kinetics

Present plasma model is developed based on the NH3 reaction mechanism proposed by Liu et al. [59]. Their model incorporates a comprehensive set of electron-impact cross sections for NH_3, calculated using the R-matrix method, along with vibrational-translational (VT)

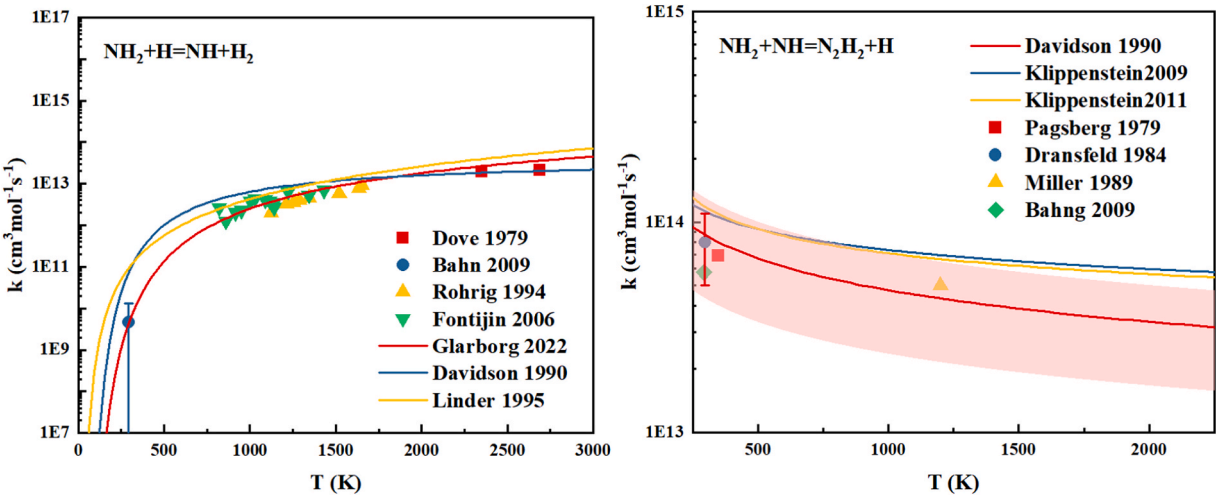

Fig. 4. Rate constant as a function of temperature. Symbols denote experiment and lines denote calculation. (a) NH_2 + H=NH + H_2. (b) NH_2 + NH=N_2H_2 + H, symbols denote experiment(Pagsberg et al. [41], Dransfeld et al. [42], Bahn et al. [42] and Miller et al. [30]) and lines denote calculation(Davidson et al. [15] and Klippenstein et al [22,25]).

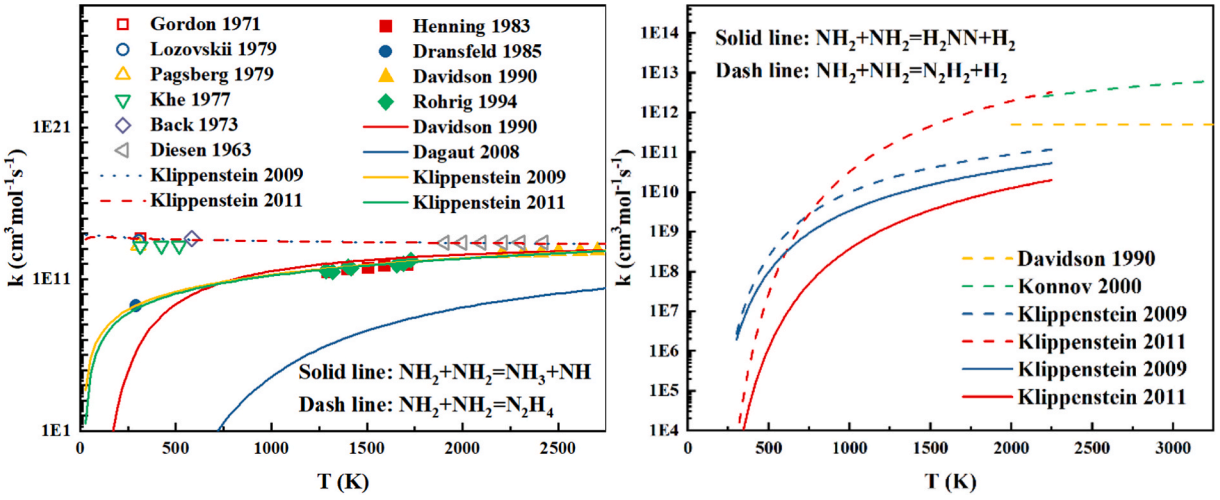

Fig. 5. Rate constant of NH_2 + NH_2 → Products as a function of temperature. Symbols denote experiment([15,42,43]-[44]) and lines denote calculation(Davidson et al. [15], Dagaut et al. [21], Konnov et al. [18] and Klippenstein et al [22,25]).

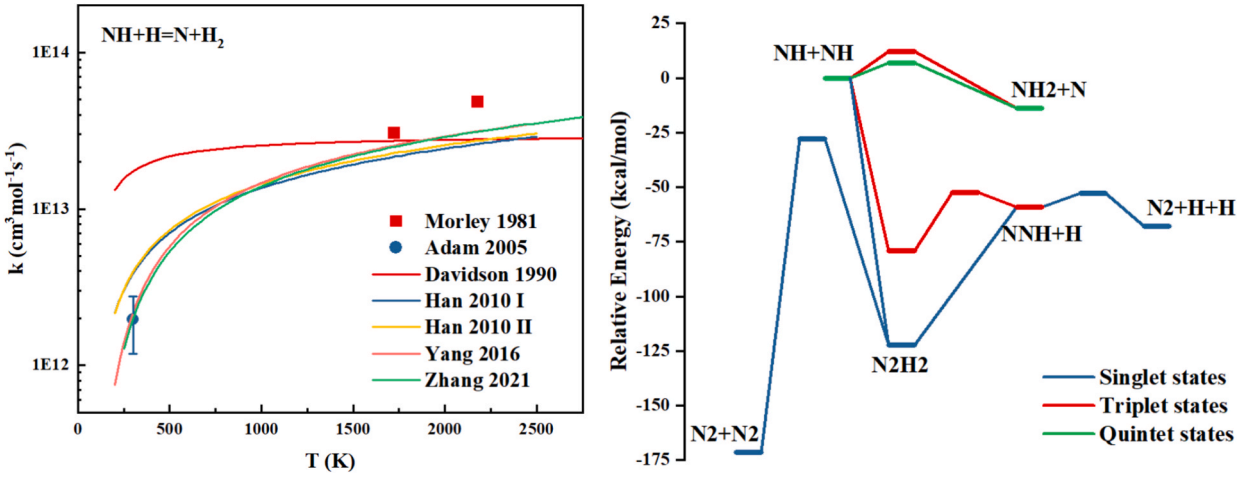

Fig. 6. (a) Rate constant of NH + H=N + H_2 as a function of temperature. Symbols denote experiment([46,47]) and lines denote calculation([15,19,26,48]). (b) Schematic of calculated energies for the reaction of NH with NH[25].

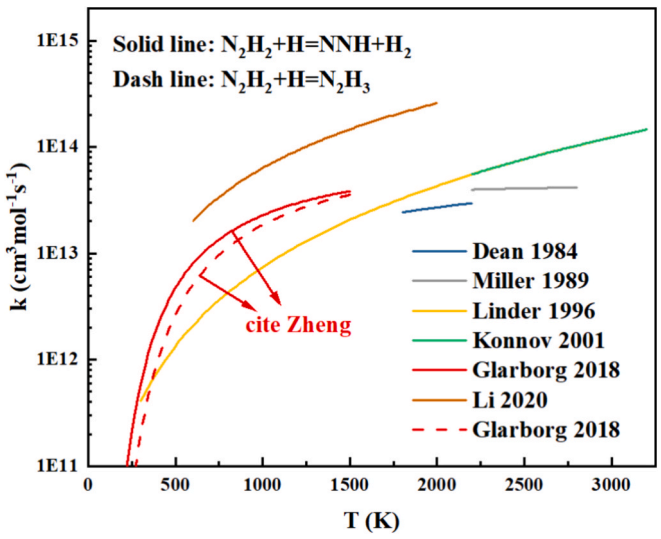

Fig. 7. Rate constant of N_2H_2 + H = products as a function of temperature: Dean et al [51], Miller et al [30],Linder et al [49], Konnov [28], Glarborg et al [23], Li et al [52].

and vibrational-vibrational (VV) relaxation rate constants derived from SSH theory. These improvements significantly enhance the accuracy of plasma-assisted NH_3 decomposition and oxidation modeling. Furthermore, as highlighted by Qiu et al. [9], electron-impact reactions involving NH_2 and NH radicals should also be considered as they are key dissociation products of NH_3. Present model incorporates these reactions, with relevant data sourced from Refs. [60] and [61]. Since H_2 is the primary product in NH_3 decomposition, we adopted the H_2-related electron-impact reactions from the works of Mao et al. [62], which utilize cross sections from the Phelps database [63] and Itikawa database [64], as well as ion-related reactions from the IST-Lisbon database [65]. Electron-impact excitation reactions, Vibrational-translational (VT) relaxation reactions, Vibrational-vibrational (VV) energy exchange reactions and Chemical reactions enhanced by vibrationally excited species were all included in Mao et al. [62], and simulations demonstrated excellent agreement with experimental data, validating the H_2 model's predictive capability. The collision cross sections for Ar and H_2 were obtained from the Phelps database [63] in the Lxcat database (see Appendix).

4. Results and discussion

4.1. Measured and predicted results

Given that the E/N ratio critically regulates energy distribution pathways and governs the formation of reactive species within plasma systems, a comprehensive investigation is required to identify the dominant active species generated across varying E/N gradients, thereby facilitating the optimization of ammonia decomposition processes.

Fig. 9(a) demonstrates the ratio of electron energy distribution during ammonia cracking process. The energy loss distribution of NH_3(v) particles exhibits a marked reduction in 10–100 Td. Within this range, the energy deposited by electrons into NH_3(v) significantly decreases, while the energy absorbed by Ar* and electronically excited NH_3 species rapidly increases. Notably, energy deposited in ions is limited. This phenomenon is desired to observe because vibrationally excited states primarily induce gas heating through collisional quenching rather than fuel decomposition. In contrast, electronically excited species Ar* directly dissociate ammonia molecules via impact reactions. The E/N ranges from 297 to 594 Td in the study of Zhang et al [6] and most of the electron energy in their conditions deposited to dissociation of NH_3 and ionization of Ar and NH_3 as their pressure is low (8 kPa). Consequently, we selected the reduced electric field strength range of 40–80 Td (highlighted in blue) in Fig. 9 (a) as the following experimental conditions. Fig. 9 (b) shows the time evolution of key radical and active particle concentrations in a single pulse for plasma-assisted NH_3 pyrolysis system at an applied voltage of 5000 V. It can be observed that NH_2 and H radicals are generated synchronously in the initial reactions of NH_3 consumption and in larger concentrations than NH radicals; vibrationally excited states quenches in the afterglow stage and rapidly converts to radicals and ions (NH_2, NH, H, NH_4^+). Following this stage, NH_4^+ (the most abundant ionic species) exhibits a gradual concentration decline, attributed to its dissociative recombination with electrons generating NH_3 alongside NH_2 and H radicals. Consequently, sustained accumulation of NH_2 and H radicals are observed throughout the reaction process.

Fig. 10 depicts the measured molar distribution of ammonia during the cracking process at applied voltages of 3500–6500 V and compares it with the simulation results of different models. Compared with the Liu et

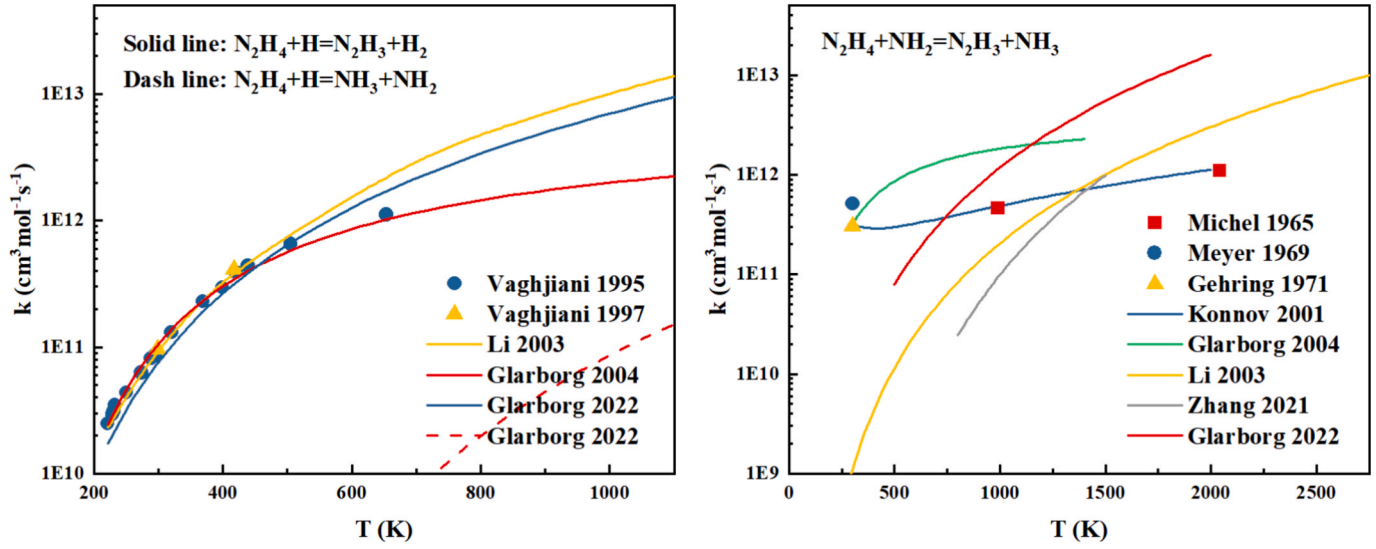

Fig. 8. (a) Rate constant of N_2H_4 + H → products as a function of temperature. Symbols denote experiment([53,54]) and lines denote calculation([23,31,55]). (b) Rate constant of N_2H_4 + NH_2 → products as a function of temperature. Symbols denote experiment([56–58]) and lines denote calculation([18,19,23,31,55]).

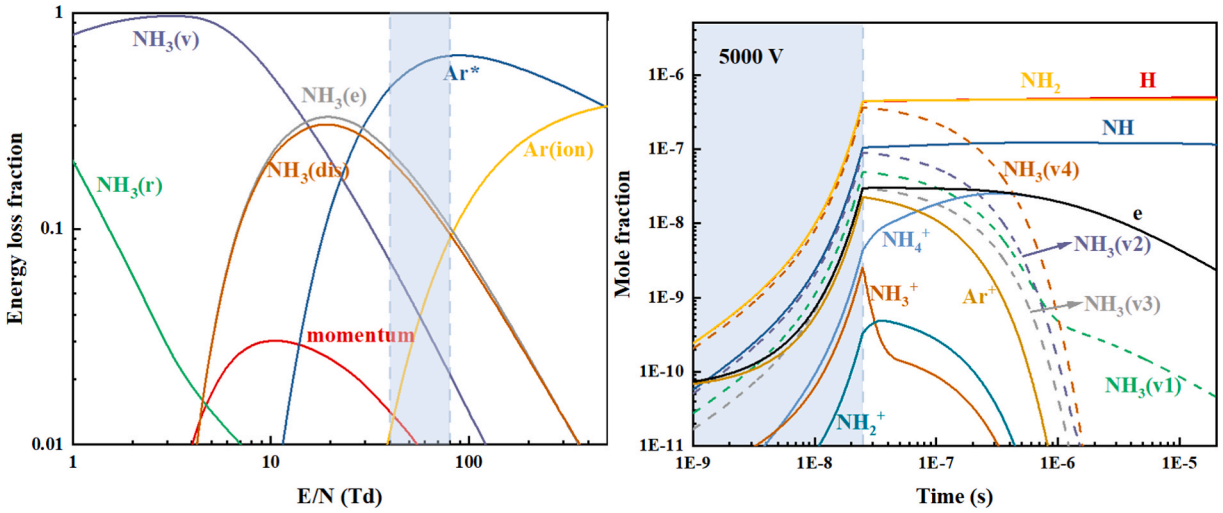

Fig. 9. (a) Energy loss fraction of gas NH_3:Ar = 0.01:0.99. (b) Time evolution of key intermediate species in a pulse.

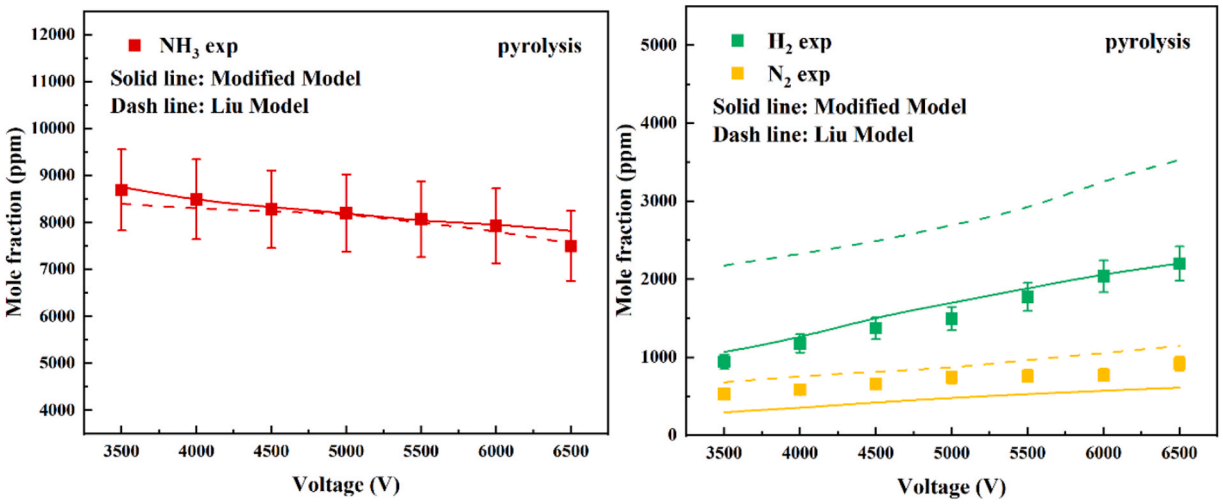

Fig. 10. Measured (symbols) and simulated (lines) mole fraction profiles of ammonia decomposition in flow reactor.

al model [59], the present modified model can predict the concentrations of NH_3 and H_2 very well, and successfully reduces the prediction error of H_2 concentration from ± 66.7 % to within ± 13.3 %, which significantly improves the problem of systematic positive bias of H_2 concentration that exists in the traditional combustion kinetic model, which was also discussed by Tamaoki et al. [66]. In the presence of plasma, ammonia can be decomposed at room temperature, with H_2 and N_2 being the main products, and simulations show that this is accompanied by products such as N_2H_2(10 ppm) and N_2H_4(200 ppm). It is important to note that once ionization of the gas has occurred by breakdown, the increase in ammonia cracking gain from continued voltage increases is not significant.

4.2. Pathway flux of NH_3

To further explore the mechanism behind the effect of plasma on ammonia consumption, as well as to study the decomposition process of NH_3, a rate of product (ROP) analysis is conducted under different voltage conditions in Fig. 11. Unlike conventional ammonia pyrolysis, NH_3 is consumed under plasma mainly through collisional reactions with excited state Ar* (R54) rather than reactions (R1) and (R2). The generation of NH_2 occurs mainly through collisions of NH_3 with the excited state of Ar* as well as with energetic electrons, which suggests that the collisional dynamics of the electrons dominates the process of NH_3 consumption and the generation of NH_2.

Increasing the voltage promotes the collisional dissociation reaction between NH_3 and Ar* (R54), while decreasing the flux of NH_3(v1-v4), which effectively promotes the decomposition of NH_3 and the increase in the concentration of the radical pool; the collisional reactions of NH_2 and NH with high-energy electrons ((R55) and (R56)) are promoted, while the addition reactions (R11) and (R15) are inhibited, thus the new reaction mechanism introduced by plasma allows more NH_2, NH and H to be generated in system.

$$NH_2 + H + M = NH_3 + M \quad \text{(R1)}$$

$$NH_3 + H = NH_2 + H_2 \quad \text{(R2)}$$

$$Ar^* + NH_3 + H \rightarrow Ar + NH_2 + 2H \quad 54)$$

$$NH_2 + e \rightarrow NH + H + e \quad 55)$$

$$NH + e \rightarrow N + H + e \quad 56)$$

$$NH_2 + NH_2 + M = N_2H_4 + M \quad 11)$$

$$NH + NH = N_2H_2 \quad 15)$$

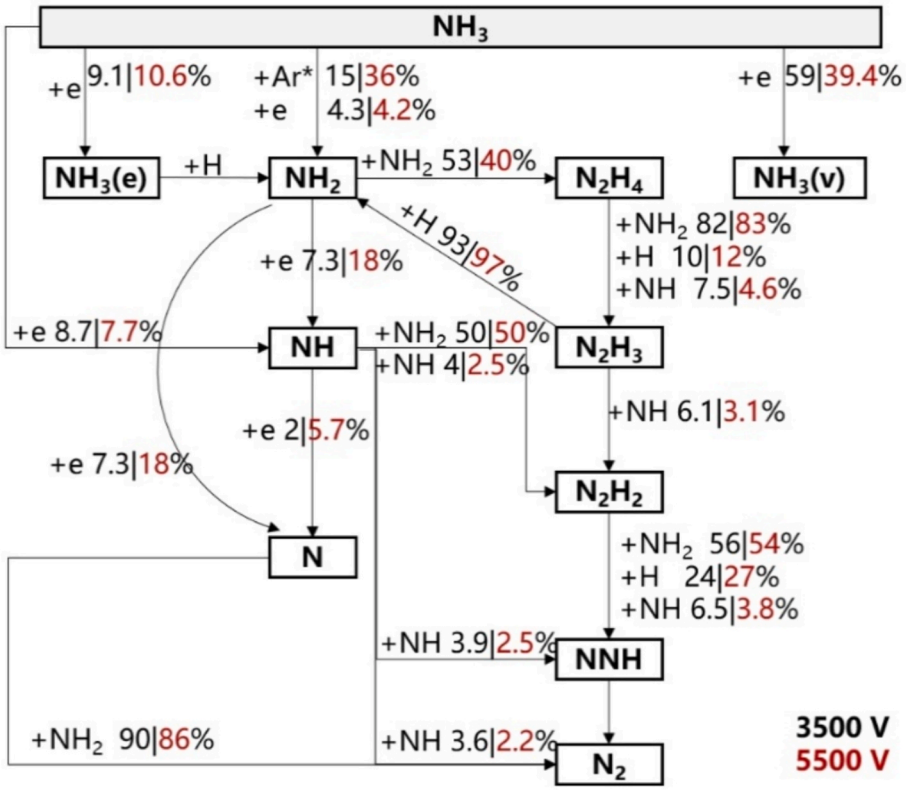

Fig. 11. The ROP analysis of NH_3 under two applied voltages (3500 V and 5500 V).

In addition to the H-abstraction reactions $NH_3 \rightarrow NH_2 \rightarrow NH \rightarrow N$, a portion of NH_2 and NH radicals participate in recombination processes, leading to the formation of N_2H_x species. Among them, N_2H_4 is generated via an addition reaction (R11), which undergoes a H-abstraction reaction (R38, R40, R41) via collisions with NH_2, H, and NH radicals to generate N_2H_3, and is ultimately converted to NNH via N_2H_2 (R21, R23, R24). Given that the lifetime of NNH is on the nanosecond timescale, the reaction (R48) rapidly attains equilibrium, followed by the subsequent decomposition of NNH into N_2 and H.

$$N_2H_4 + H = NH_3 + NH_2 \quad 38)$$

$$N_2H_4 + NH = N_2H_3 + NH_2 \quad 40)$$

$$N_2H_4 + NH_2 = N_2H_3 + NH_3 \quad 41)$$

$$N_2H_3 + NH = N_2H_2 + NH_2 \quad 31)$$

$$N_2H_2 + NH_2 = NNH + NH_3 \quad 24)$$

$$N_2H_2 + NH = NNH + NH_2 \quad 33)$$

$$N_2H_2 + H = NNH + H_2 \quad 21)$$

$$NNH = N_2 + H \quad 48)$$

Fig. 12 compares the formation and consumption pathways of H_2 under different voltages. Within the operating conditions investigated in this study, H_2 is primarily generated through the electron-impact dissociation of NH_3 (R57), which differs from conventional H_2 formation pathways. Although H_2 can be excited to vibrational and electronic states through collisions with electrons, the focus of this study remains on its formation process, as H_2 does not participate as a reactant in the considered reactions.

$$NH_3 + e \rightarrow NH + H_2 + e \quad 57)$$

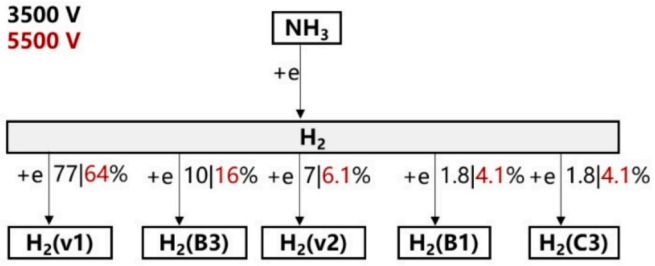

Fig. 12. The ROP analysis of H_2 under two applied voltages (3500 V and 5500 V).

$$NH_3 + e \rightarrow NH_2 + H + e \quad 58)$$

The sensitivity analysis of NH_3 and H_2 are shown in Fig. 13. A positive sensitivity coefficient indicates that doubling the reaction rate would increase the species concentration, while a negative value suggests a decrease. Through sensitivity calculations, the key reactions governing NH_3 consumption are identified. At both voltages, the reactions $NH_3 + e \rightarrow NH_3^+ + 2e$ and $Ar + e \rightarrow Ar^+ + 2e$ exhibit significant sensitivity coefficients. As the voltage increases, the importance of $Ar + e \rightarrow Ar^* + e$ becomes more pronounced. This is because higher electric field excites more Ar* species, which subsequently enhance NH_3 consumption. The sensitivity analysis of H_2 reveals that $Ar + e \rightarrow Ar^+ + 2e$ plays the most critical role in H_2 production. This reaction ionizes ground Ar to generate additional electrons, triggering an electron avalanche effect that simultaneously promotes NH_3 decomposition and H_2 formation. Conversely, the recombination reaction between NH_4^+ ions and electrons ($NH_4^+ + e \rightarrow NH_3 + H$) negatively impacts H_2 generation. This is because it consumes high-energy electrons to reform NH_3, thereby reducing the availability of electrons for NH_3 decomposition into H_2.

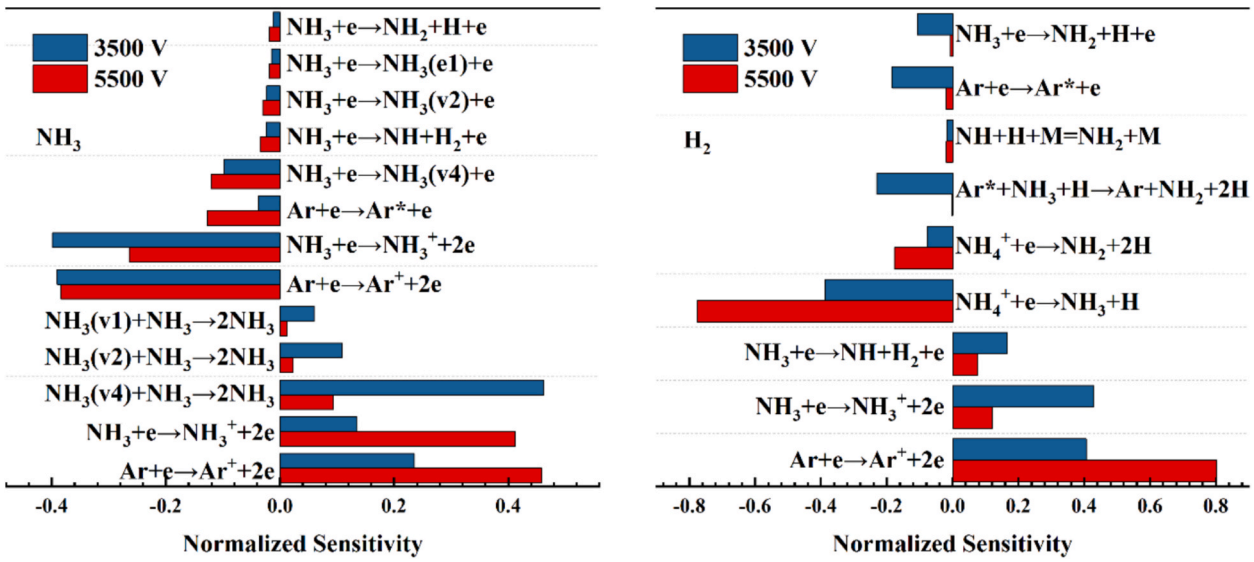

Fig. 13. Sensitivity analysis for NH_3 and H_2 under 3500 V and 5500 V.

In this work, Ar plays a crucial role in the ammonia decomposition process. Ar* is easily formed and mainly reacts with NH_3 to produce H and NH_2 radicals that boost system's radical concentration. The following illustrates the transformation process in the Ar system shown in Fig. 14. Under the influence of the electric field, Ar is initially excited to Ar* through collisions with high-energy electrons (R59), subsequently participating in fuel consumption reactions (R54). Simultaneously, a small fraction of Ar is ionized to ionic Ar^+ (R60), which then interacts with fuel molecules, converting NH_3 into NH_2^+ ions and H radicals through collision processes (R61).

$$Ar + e \rightarrow Ar^* + e \quad (59)$$

$$Ar + e \rightarrow Ar^+ + e + e \quad (60)$$

$$Ar^+ + NH_3 + H \rightarrow Ar + NH_2^+ + 2H \quad (61)$$

4.3. Effects of key particles

Fig. 15 compares the concentrations of key particles at different voltages. After the applied voltage is increased from 3500 V to 5500 V, the concentration of H radicals increases by a factor of 3, accompanied by an increase in the concentration of NH_2 radicals. N_2H_4 shows the highest mole fraction among N_2-products, increases by a factor of 10. And N_2H_2 concentration rises by a factor of 3. In contrast, NNH maintains the lowest concentration due to its high reactivity which readily converts into N_2 and H atom. Thus, the plasma greatly facilitates the generation of reactive radicals in the system and drives ammonia decomposition.

Fig. 16 illustrates the pathways and fluxes for the generation and consumption of H radicals. H is mainly generated through dissociation reactions of NH_3 with Ar* and electron collisions, accompanied by the generation of NH_2.The generated H radicals is consumed through hydrogenation reactions with N_2H_3 and hydrogen abstraction reactions with the excited state NH_3(e).

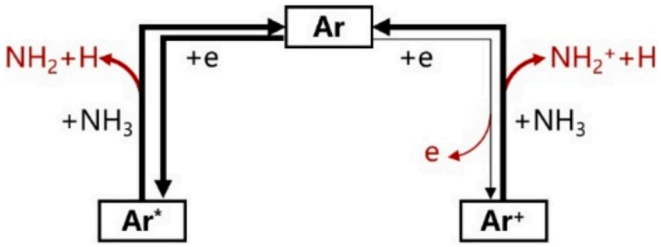

Fig. 14. The ROP analysis of Ar.

5. Conclusion

This work conducted a synergistic experimental and modeling study for non-equilibrium plasma chemistry in dielectric barrier discharge (DBD) reactors, specifically targeting ammonia decomposition. Species profiles of key species were measured and a new kinetic model is developed to more precisely predict the ammonia decomposition at low temperature with plasma assisted. This modified model incorporates more accurate rate constants, and an optimized plasma-coupled mechanism is integrated. Systematic validation against concentration profiles revealed improvement in predictive accuracy over conventional combustion kinetic models, with radical flux analysis identifying the concrete mechanism of NH_3 decomposition.

The plasma-driven decomposition mechanism is fundamentally governed by synergistic interactions between excited Ar* species and energetic electrons. Notably, the initiation of NH_3 decomposition is predominantly driven by electron impact dissociation ($e + NH_3 \rightarrow NH_2 + H + e$) and Ar* collisional activation ($Ar^*+H + NH_3 \rightarrow NH_2 + 2H + Ar$). Hydrogen production is critically dominated (more than 95 % flux contribution) by direct electron impact on NH_3 ($e + NH_3 \rightarrow NH + H_2 + e$). The high-energy Ar* species play a key role as energy carrier (11.55 eV) and reactive collision partner facilitating energy transfer via quenching-induced dissociation pathways. Formation of N_2H_4 proceeds through NH_2 dimerization ($NH_2 + NH_2 = N_2H_4$), followed by sequential dehydrogenation via H-abstraction ($N_2H_4 + H = N_2H_3 + H_2$, etc.) ultimately yielding molecular nitrogen.

CRediT authorship contribution statement

Shuming Li: Writing – original draft. **Huanrui Guo:** Data curation. **Geyuan Yin:** Writing – review & editing. **Erjiang Hu:** Writing – review & editing, Funding acquisition. **Zuohua Huang:** Supervision, Conceptualization.

Declaration of competing interest

The authors declare that they have no known competing financial interests or personal relationships that could have appeared to influence

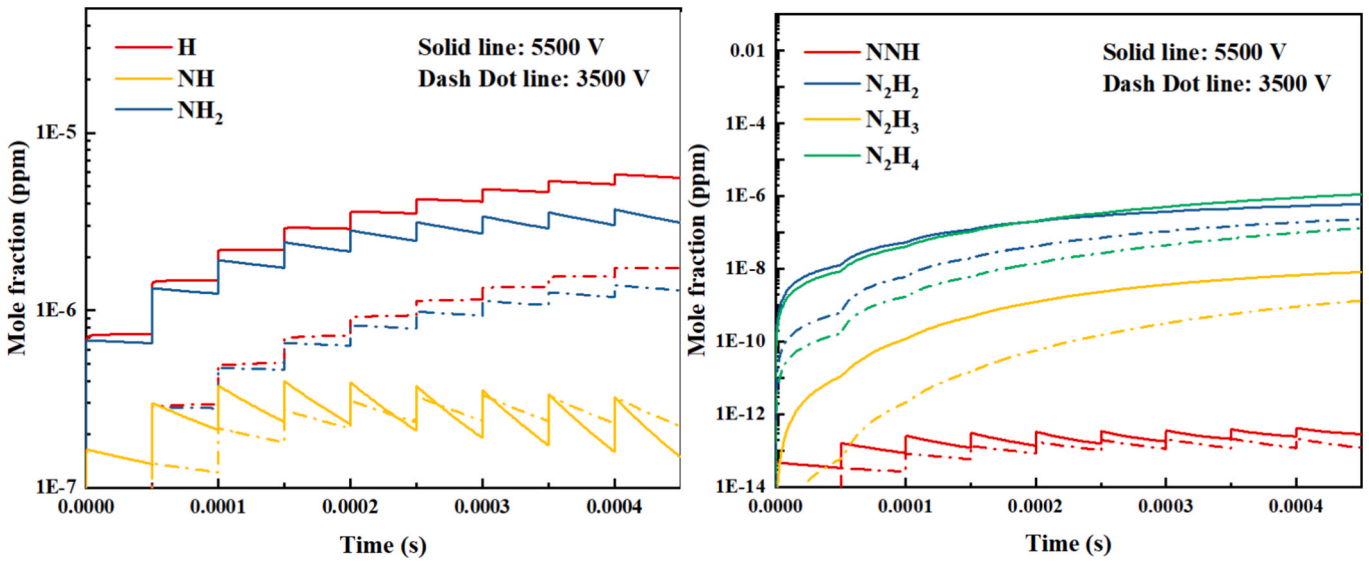

Fig. 15. Mole fraction of key particles at different voltages.

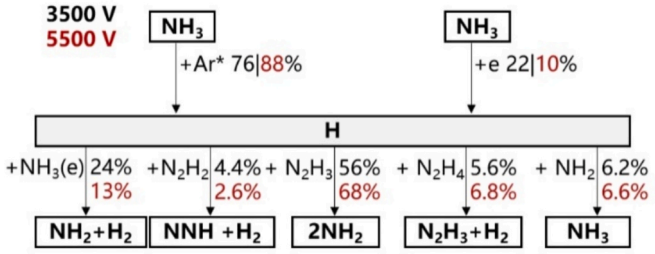

Fig. 16. The ROP analysis of H under two applied voltages (3500 V and 5500 V).

the work reported in this paper.

Acknowledgements

This study was supported by the National Natural Science Foundation of China (52176131, 52476128), the Advanced Jet Propulsion Innovation Center Construction (HKCX-220224-01-22). Natural Science Foundation of Shaanxi Province (2021JLM-18, 2020JC-04, 2023KXJ-228), National Science and Technology Major Project (J2019-III-0004-0047).

Appendix A. Supplementary data

Supplementary data to this article can be found online at https://doi.org/10.1016/j.fuel.2025.136427.

Data availability

Data will be made available on request.

References

[1] Meng X, Liu L, Qin M, Miao M, Zhao H, Long W, et al. Study on ammonia/methanol blends with ammonia cracking for low-carbon combustion and NO reduction. J Clean Prod 2024;450:141959. https://doi.org/10.1016/j.jclepro.2024.141959Get. rights and content.

[2] Mercer E, Alphen S, Deursen C, Righart T, Bongers W, Sntders R, Peeters F. Post-plasma quenching to improve conversion and energy efficiency in a CO_2 microwave plasma. Fuel 2023;334:126734. https://doi.org/10.1016/j.fuel.2022.126734.

[3] Alexander F, Frank L, Yukihiro K, Bjarne S, Erekle T, Henrik B. Plasma Chemistry in an Atmospheric pressure Ar/NH3 Dielectric Barrier Discharge. Plasma Processes Polym 2006;2(3):193–200. https://doi.org/10.1002/ppap.200400051.

[4] Choe J, Sun W, Ombrello T, Carter C. Plasma assisted ammonia combustion: Simultaneous NOx reduction and flame enhancement. Combust Flame 2021;228:430–2. https://doi.org/10.1016/j.combustflame.2021.02.016.

[5] Zhong H, Mao X, Ning L, Wang Z, Ombrello T, Ju Y. Understanding non-equilibrium N2O/NOx chemistry in plasma-assisted low-temperature NH_3 oxidation. Combustion and Flame 2023;256:112948.https://doi.org/10.1016/j.combustflame.2023.112948.

[6] Zhang M, Chen Q, Zhou G, Sun J, Lin H. Low-temperature chemistry in plasma-driven ammonia oxidative pyrolysis. Green Energy and Environment 2024;9(9):1477–88. https://doi.org/10.1016/j.gee.2023.05.010.

[7] Glarborg P, Miller J, Ruscic B, Klippenstein S. Modeling nitrogen chemistry in combustion. Prog Energy Combust Sci 2018;67:31–68. https://doi.org/10.1016/j.pecs.2018.01.002.

[8] Mao X, Chen Q, Guo C. Methane pyrolysis with N2/Ar/He diluents in a repetitively-pulsed nanosecond discharge: Kinetics development for plasma assisted combustion and fuel reforming. Energ Conver Manage 2019;200:1122018. https://doi.org/10.1016/j.enconman.2019.112018.

[9] Qiu Y, Zhu Y, Wu Y, Zhao N, Li Z, Hao M, et al. Numerical investigation of the hybrid pulse–DC plasma assisted ignition and NOx emission of NH_3/N2/O2 mixture. Combust Flame 2023;258:113078. https://doi.org/10.1016/j.combustflame.2023.113078.

[10] http://www.zdplaskin.laplace.univ-tlse.fr/.

[11] Lutz A, Kee R, Miller J, SENKIN: A Fortran program for predicting homogeneous gas phase chemical kinetics with sensitivity analysis, https://www.osti.gov/biblio/5371815, 1987.

[12] Lefkowitz J, Guo P, Rousso A, Ju Y. Species and temperature measurements of methane oxidation in a nanosecond repetitively pulsed discharge. Philosophical Transactions A 2015;373(2048):20140333. https://doi.org/10.1098/rsta.2014.0333.

[13] Hagelaar G, Pitchford L. Plasma Sources Sci Technol 2005;14:722–33.

[14] S.A. Alturaifi O. Mathieu E.L. Petersen An experimental and modeling study of ammonia pyrolysis Combust Flame 2021; 111694.https://doi.org/10.1016/j.combustflame.2021.111694.

[15] Davidson D, Kohse-Hoeinghaus K. Chang a.a pyrolysis mechanism for ammonia. Int J Chem Kinet 1990;22(5):513–35. https://doi.org/10.1002/kin.550220508.

[16] Otomo J, Koshi M, Mitsumori T, Iwasaki H, Yamada K. Chemical kinetic modeling of ammonia oxidation with improved reaction mechanism for ammonia/air and ammonia/hydrogen/air combustion. Int J Hydrogen Energy 2018;S0360319917347055. https://doi.org/10.1016/j.ijhydene.2017.12.066.

[17] Song Y, Hashemi H, Christensen JM, Zou C, Marshall P, Glarborg P. Ammonia oxidation at high pressure and intermediate temperatures. Fuel 2016;181:358–65. https://doi.org/10.1016/j.fuel.2016.04.100.

[18] Konnov A, Ruyck J. Kinetic Modeling of the thermal Decomposition of Ammonia. Combust Sci Technol 2000;152(1):23–37. https://doi.org/10.1016/j.ijhydene.2017.12.066.

[19] Zhang X, Moosakutty S, Rajan R, Younes M, Sarathy S. Combustion chemistry of ammonia/hydrogen mixtures: Jet-stirred reactor measurements and comprehensive kinetic modeling. Combust Flame 2021;234:111653. https://doi.org/10.1016/j.combustflame.2021.111653.

[20] Mathieu O, Petersen E. Experimental and modeling study on the high-temperature oxidation of Ammonia and related NOx chemistry. Combust Flame 2015;162(3):554–70. https://doi.org/10.1016/j.combustflame.2014.08.022.

[21] Dagaut P, Glarborg P, Alzueta M. The oxidation of hydrogen cyanide and related chemistry. Prog Energy Combust Sci 2008;34(1):1–46. https://doi.org/10.1016/j.pecs.2007.02.004.

[22] Klippenstein S, Harding L, Glarborg P, Miller J. The role of NNH in NO formation and control. Combust Flame 2011;158(4):774–89. https://doi.org/10.1016/j.combustflame.2010.12.013.

[23] Glarborg P, Hashemi H, Marshall P. Challenges in Kinetic Modeling of Ammonia Pyrolysis. Fuel Commun 2022. https://doi.org/10.1016/j.jfueco.2022.100049.

[24] Ko T, Marshall P, Fontijn A. Rate coefficients for the hydrogen atom + ammonia reaction over a wide temperature range. J Phys Chem 1990;94(4):1401–4. https://doi.org/10.1021/j100367a037.

[25] Linder DP, Duan X, Page M. Ab Initio Variational transition State Theory Calculations for the H +NH2 =H2 +NH Hydrogen Abstraction Reaction on the Triplet potential Energy Surface. J Phys Chem 1995;99:11458–63. https://doi.org/10.1021/j100029a025.

[26] Yang H, Zheng Y, Ge M. Effects of initial rotational quantum state excitations and thermal rate coefficient at room temperature for the H(2S)+NH(X3∑)→N (4S)+ H2(X1∑+g) reaction. Theor Chem Acc 2016:135. https://doi.org/10.1007/s00214-016-1823-y.

[27] Dean A M, Bozzelli J W. Combustion Chemistry of Nitrogen. Springer New York 2000. https://doi.org/10.1007/978-1-4612-1310-9_2.

[28] Konnov AA, Ruyck JD. Kinetic modeling of the decomposition and flames of hydrazine. Combust Flame 2001;124(1):106–26. https://doi.org/10.1016/S0010-2180(00)00187-5.

[29] Pascal D, Catoire L. Contributions of Experimental Data Obtained in Concentrated Mixtures to Kinetic Studies: Application to Monomethylhydrazine Pyrolysis. Chem A Eur J 2020;124(30). https://doi.org/10.1021/acs.jpca.0c03144.

[30] Miller JA, Smooke MD, Green RM, Kee RJ. Kinetic Modeling of the Oxidation of Ammonia in Flames. Combust Sci Technol 1983;34(1–6):149–76. https://doi.org/10.1080/00102208308923691.

[31] Skreiberg Y, Kilpinen P, Glarborg P. Ammonia chemistry below 1400 K under fuel-rich conditions in a flow reactor. Combust Flame 2004;136(4):501–18. https://doi.org/10.1016/j.combustflame.2003.12.008.

[32] Michael J, Sutherland J, Klemm R. The flash photolysis-shock tube technique using atomic resonance absorption for kinetic studies at high temperatures. Int J Chem Kinet 1985;17:315–26. https://doi.org/10.1002/kin.550170308.

[33] Michael J, Sutherland J, Klemm R. Rate constant for the reaction, atomic hydrogen +ammonia, over the temperature range, 750-1777 K. J Phys Chem 1986;90:497–500. https://doi.org/10.1021/j100275a029.

[34] Corchado J, Espinos J. Analytical potential energy surface for the NH3+ H↔NH2+ H2 reaction: application of variational transition-state theory and analysis of the equilibrium constants and kinetic isotope effects using curvilinear and rectilinear coordinates. J Chem Phys 1997;106:4013–21. https://doi.org/10.1063/1.473119.

[35] Yang M, Corchado J. Seven dimensional quantum dynamics study of the H2+ NH2→H+NH3 reaction. J Chem Phys 2007;127:184308. https://doi.org/10.1063/1.2790902.

[36] Espinosa J, Corchado J. Analytical potential energy surface and kinetics of the NH3 +H→NH2+H2 hydrogen abstraction and the ammonia inversion reactions. J Phys Chem 2010;114:4455–63. https://doi.org/10.1063/1.2790902.

[37] Deppe J, Friedrichs G, Ibrahim A, Wagner H. The thermal Decomposition of NH2 and NH Radicals. Ber Bunsenges Phys Chem 1998;102:1474–85. https://doi.org/10.1002/bbpc.199800016.

[38] Bahng M, Macdonald R. Determination of the Rate Constants for the RadicalRadical Reactions NH2(X2B1) + NH(X3Σ) and NH2(X2B1) + H(2S) at 293 K. Chem A Eur J 2009;113(11):2415–23. https://doi.org/10.1021/jp809643u.

[39] Fontijn A, Shamsuddin S, Crammond D, Marshall P, Anderson W. Kinetics of the NH reaction with H2 and reassessment of HNO formation from NH +CO2, H2O. Combust Flame 2006;145:543–51. https://doi.org/10.1016/j.combustflame.2005.12.012.

[40] Dove J, Nip W. A shock-tube study of ammonia pyrolysis. Can J Chem 1979;57:689–701. https://doi.org/10.1139/v79-11.

[41] Pagsberg P, Eriksen J, Christensen H. Pulse radiolysis of gaseous ammonia-oxygen mixtures. J Phys Chem 1979;83:582–90. https://doi.org/10.1021/j100468a006.

[42] P. Dransfeld W. Hack H. Kurzke F. Temps H.G. Wagner Direct studies of elementary reactions of NH2-radicals in the gas phase Symp (Int) Combust 20 1985 655 663 10.1016/S0082-0784(85)80555-5.

[43] Diesen RW. Mass spectral studies of kinetics behind shock waves. II. thermal decomposition of hydrazine. J Chem Phys 1963;39:2121–8. https://doi.org/10.1063/1.1701411.

[44] Hennig G, Rohrig M, Gg WH. About the rate of the reaction of NH(X3Σ) with O2 over a large temperature range. Ber Bunsen Ges Phys Chem 1993;97:830–2. https://doi.org/10.1002/bbpc.19930970613.

[45] Meng X, Liu L, Qin M, Zhu W, Long W, Bi M. Modeling and chemical kinetic analysis of methanol and reformed gas (H2/CO2) blending with ammonia under lean-burn condition. Int J Hydrogen Energy 2024;58:190–9. https://doi.org/10.1016/j.ijhydene.2024.01.150.

[46] Morley C. The mechanism of no formation from nitrogen compounds in hydrogen flames studied by laser fluorescence. Symposium (Int) Combust 1981;18:23–32. https://doi.org/10.1016/S0082-0784(81)80007-0.

[47] Adam L, Hack W, Zhu H, Qu ZW, Schinke R. Experimental and theoretical investigation of the reaction NH(X3Σ)+H(2S)–>N(4S)+H2(X1Σ+g). J Chem Phys 2005;122:114301. https://doi.org/10.1063/1.1862615.

[48] Han B, Yang H, Zheng Y, Varandas AJC. Quasi-classical trajectory and quantum mechanics study of the reaction H(2S)+NH→N(4S)+H2. Chem Phys Lett 2010;493:225–8. https://doi.org/10.1016/j.cplett.2010.05.049.

[49] Linder D, Duan X, Page M. Thermal rate constants for R+N2H2→RH+N2H (R=H, OH, NH2) determined from multireference configuration interaction and variational transition state theory calculations. J Chem Phys 1996;104(16):6298–307. https://doi.org/10.1063/1.471290.

[50] Zheng J, Rocha R, Pelegrini M, Ferrao L, Carvalho E, Orlando N, et al. A product branching ratio controlled by vibrational adiabaticity and variational effects: Kinetics of the H + trans-N2H2 reactions. J Chem Phys 2012;136:184310. https://doi.org/10.1063/1.4707734.

[51] Dean A, Chou M, Stern D. Kinetics of rich ammonia flames. Int J Chem Kinet 1984;16(6):633–53. https://doi.org/10.1002/kin.550160603.

[52] Li Y, Sarathy SM. Probing hydrogen–nitrogen chemistry: a theoretical study of important reactions in NxHy, HCN and HNCO oxidation. Int J Hydrogen Energy 2020;45(43). https://doi.org/10.1016/j.ijhydene.2020.06.083.

[53] Vaghjiani GL. Laser photolysis studies of hydrazine vapor: 193 and 222-nm H-atom primary quantum yields at 296 K, and the kinetics of H + N2H4 reaction over the temperature range 222-657 K. Int J Chem Kinet 1995;27(8):777–90. https://doi.org/10.1002/kin.550270805.

[54] Vaghjiani GL. UV absorption cross sections, laser photodissociation product quantum yields, and reactions of H atoms with methylhydrazines at 298 K. J Phys Chem A 1997;**101**:4167–71.https://doi.org/10.1021/jp964044z.

[55] Li QS, Zhang X, Zhang SW. Direct dynamics study on the hydrogen abstraction reaction N2H4+H→N2H3+H2. Chem A Eur J 2003;107(31):6055–61. https://doi.org/10.1021/jp034592u.

[56] Gehring V, Hoyermann K, Gg W, Wolfram J. Die Reaktion von atomarem Wasserstoff mit Hydrazin. Ber Bunsenges Phys Chem 1971;75:1287. https://doi.org/10.1002/bbpc.197100005.

[57] Meyer E, Olschewski HA, Troe J, Wagner HG. Investigation of N2H4 and H2O2 decomposition in low and high pressure shock waves. Symp Combust 1969;12(1):345–55. https://doi.org/10.1016/S0082-0784(69)80417-0.

[58] Michel K, Wagner H. The pyrolysis and oxidation of hydrazine behind shock waves. Symp Combust 1965;10(1):353–64. https://doi.org/10.1016/S0082-0784(65)80182-5.

[59] Liu N, Chen H, Zhang M, Chen Q, Jiang X, Yang B. Kinetic insights into nanosecond pulsed plasma assisted NH3/O2/Ar ignition with R-matrix cross section. Combust Flame 2024;267(000):11. https://doi.org/10.1016/j.combustflame.2024.113571.

[60] Hayashi M. Electron collision cross-sections determined from beam and swarm data by Boltzmann analysis. Nonequilib Process Partial Ioniz Gases 1990;220:333–40. https://doi.org/10.1007/978-1-4615-3780-9_21.

[61] Tarnovsky V, Deutsch H, Becker K. Cross-sections for the electron impact ionization of NDx (x =1−3). Int J Mass Spectrom Ion Process 1997;167–168(69–78). https://doi.org/10.1016/S0168-1176(97)00033-5.

[62] Mao X, Chen Q, Rousso A, Chen T, Ju Y. Effects of controlled non-equilibrium excitation on H2/O2/He ignition using a hybrid repetitive nanosecond and DC discharge. Combust Flame 2019;206:522–35. https://doi.org/10.1016/j.combustflame.2019.05.027.

[63] Phelps database. www.lxcat.net, retrieved on January 15, 2025.

[64] Itikawa database. www.lxcat.net, retrieved on January 15, 2025.

[65] IST-Lisbon database. www.lxcat.net, retrieved on January 15, 2025.

[66] Tamaoki K, Murakami YK, Kanayama K, Tezuka T. Roles of NH_2 reactions in ammonia oxidation at intermediate temperatures: Experiments and chemical kinetic modeling. Combustion and Flame 2024;259:113177.https://doi.org/10.1016/j.combustflame.2023.113177.